ACS Catalysis

pubs.acs.org/acscatalysis Research Article

Atomic-Level Understanding for the Enhanced Generation of Hydrogen Peroxide by the Introduction of an Aryl Amino Group in Polymeric Carbon Nitrides

Tong Zhang, Waldemar Schilling, Shahid Ullah Khan, H. Y. Vincent Ching, Can Lu, Jianhong Chen, Aleksander Jaworski, Giovanni Barcaro, Susanna Monti, Karolien De Wael, Adam Slabon, and Shoubhik Das*

Cite This: https://doi.org/10.1021/acscatal.1c03733 Read Online

ACCESS | Metrics & More | Article Recommendations | Supporting Information

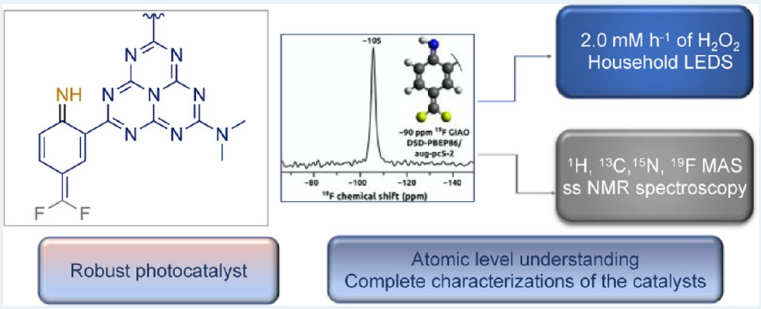

ABSTRACT: Heterogeneous catalysts are often "black boxes" due to the insufficient understanding of the detailed mechanisms at the catalytic sites. An atomic-level elucidation of the processes taking place in those regions is, thus, mandatory to produce robust and selective heterogeneous catalysts. We have improved the description of the whole reactive scenario for polymeric carbon nitrides (PCN) by combining atomic-level characterizations with magic-angle spinning (MAS) solid-state nuclear magnetic resonance (NMR) spectroscopy, classical reactive molecular dynamics (RMD) simulations, and quantum chemistry (QC) calculations. We disclose the structure−property relationships of an ad hoc modified PCN by inserting an aryl amino group that turned out to be very efficient for the production of H_2O_2. The main advancement of this work is the development of a difluoromethylene-substituted aryl amino PCN to generate H_2O_2 at a rate of 2.0 mM·h^{-1} under the irradiation of household blue LEDs and the identification of possible active catalytic sites with the aid of ^{15}N and ^{19}F MAS solid-state NMR without using any expensive labeling reagent. RMD simulations and QC calculations confirm and further extend the experimental descriptions by revealing the role and locations of the identified functionalities, namely, NH linkers, $-NH_2$ terminal groups, and difluoromethylene units, reactants, and products.

KEYWORDS: *atomic-level characterizations, hydrogen peroxide, aryl amino PCNs, ^{15}N and ^{19}F solid-state NMR spectroscopy, O_2 reduction*

INTRODUCTION

Heterogeneous catalysts are essential for industrial synthesis because of their easy separation and reusability.[1] However, still the traditional catalysts are poorly characterized and classified in terms of their active catalytic sites.[2] A clear understanding of these fundamental regions is essential to obtain a robust heterogeneous catalyst and to improve the structure−activity relationships of the whole process. Among the heterogeneous catalysts, polymeric carbon nitrides (PCN) have attracted much attention as metal-free catalysts with an appropriate band structure for various applications, such as water splitting, oxygen reduction reactions, C−C bond cleavage reactions, etc.[3,4] Advantageously, fabrications and modifications of PCN are also feasible, and strategies such as morphology tuning,[5] defect control,[6,7] elemental doping,[8,9] and hybridization[10] have been intensively investigated. Despite these improvements, characterization and structure determination of the active sites still remain inadequately explored. Although great efforts have been made to disclose the active site region by scanning transmission electron microscopy with energy-dispersive X-ray spectroscopy (STEM EDX) mapping, the discrimination between carbon and

Received: August 17, 2021
Revised: October 5, 2021

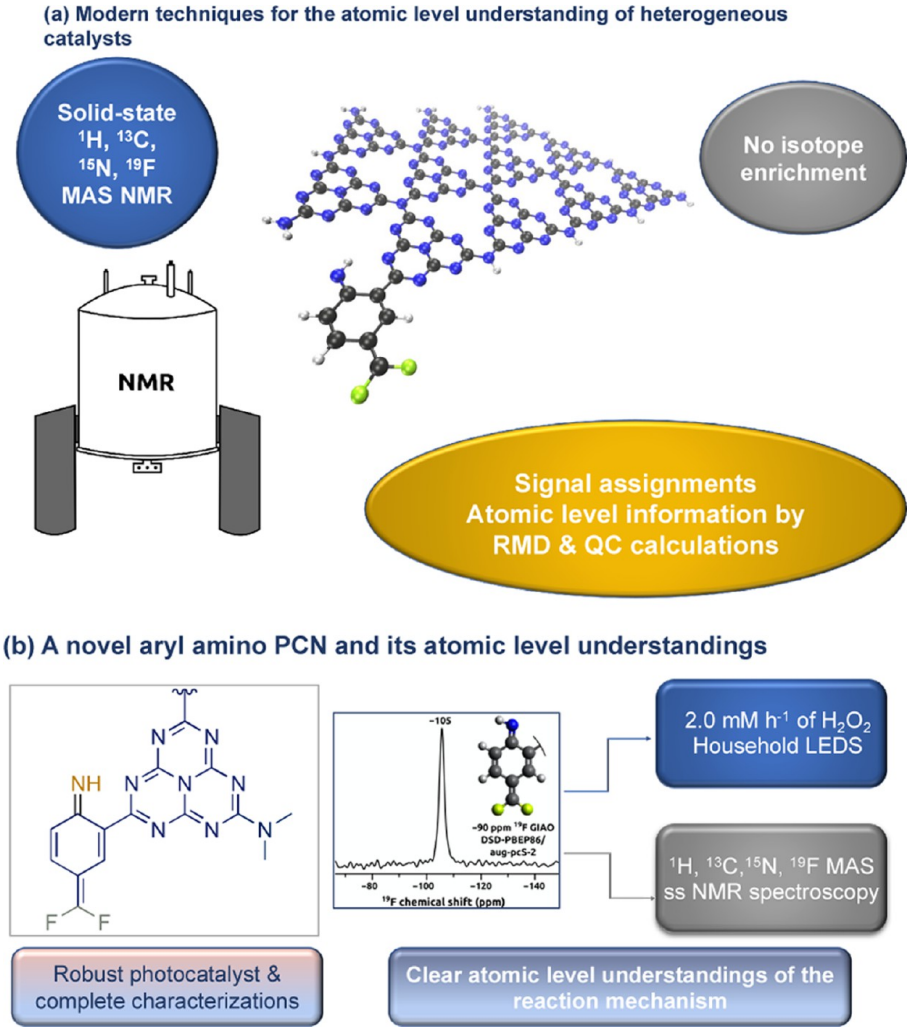

Figure 1. Atomic-level characterizations of the aryl amino PCN photocatalyst for the generation of H_2O_2.

nitrogen is still very difficult due to their close positions in the periodic table.

This problem can be potentially overcome by a combination of experimental techniques and computational methodologies. On the one hand, solid-state NMR spectroscopy can be very efficient for its atomic selectivity and ability to depict the local chemical environments regardless of the chemical/structural disorder or low species concentration. Indeed, among the nuclei relevant for this study, nitrogen is the most challenging one. This is because the NMR active isotope ^{14}N exhibits severe spectral broadening due to quadrupolar interaction[11] (with exceptions for highly symmetric environments), and the other active isotope ^{15}N suffers from low natural abundance and, therefore, sensitivity, which often requires isotope enrichment. However, it has been shown that ^{15}N NMR is capable of delivering crucial information for the nitrogen inserted in materials.[12] The catalyst examined here is appropriate for cross-polarization (CPMAS) NMR experiments at the natural ^{15}N-isotope abundance due to the presence of protons (Figure 1a).

On the other hand, reactive molecular dynamics simulations (ReaxFF flavor[13]) of these types of materials, based on efficient preparametrized potentials,[14] are a powerful tool to explore the most probable interactions and locations of the different species present in the complex environment in where the catalyst is inserted, to reproduce reaction mechanisms realistically and, in conjunction with the nudged elastic band (NEB) approach, at the QC level, identify key intermolecular interactions driving the reactants to crucial intermediates and products.[15]

Given these premises, we focused on the development of a novel metal-free heterogeneous photocatalyst for the production of hydrogen peroxide (H_2O_2). This is because hydrogen peroxide is considered one of the 100 most essential chemicals.[16] The current global market size for H_2O_2 has reached 1.49 billion USD with a compound annual growth rate (CAGR) forecast of more than 4.7% from 2020 to 2027.[17] Currently, more than 95% of the total industrial production of H_2O_2 relies on the anthraquinone oxidation (AO) process, which suffers from several drawbacks such as the use of an explosive gas mixture of H_2 and O_2, high energy consumption, and capital investments.[18]

Therefore, there is an urgent need to develop new methods for the production of H_2O_2 under mild reaction conditions. To date, various photoactive materials have been investigated for photocatalytic H_2O_2 production.[19−31] For example, Fukuzumi et al. reported a photocatalytic process for the production of H_2O_2 from water and oxygen using a mixture of

https://doi.org/10.1021/acscatal.1c03733
ACS Catal. XXXX, XXX, XXX−XXX

Table 1. Reported PCNs for the Generation of H_2O_2 Using a Mixture of Water and Alcohols

entry	material	sacrificial reagent	light source[a]	H_2O_2 production rate[c]	references
1	g-C_3N_4	ethanol[d]	2 kW Xe lamp	0.53 mM·h^{-1}	32
2	mesoporous g-C_3N_4	ethanol[d]	2 kW Xe lamp	0.83 mM·h^{-1}	33
3	(K, P, O)-g-C_3N_4	ethanol[e]	300 W Xe arc lamp	0.23 mM·h^{-1}	34
4	CoP/g-C_3N_4	ethanol[e]	300 W Xe lamp	0.07 mM·h^{-1}	35
5	Au/g-C_3N_4	2-propanol[f]	300 W Xe lamp	0.47 mM·h^{-1}	36
6	3DOM g-C_3N_4-PW_{11}	organic electron donors	300 W Xe lamp[b]	0.42 mM·h^{-1}	37
7	AQ-augmented g-C_3N_4	2-propanol[e]	150 W Xe arc lamp	0.18 mM·h^{-1}	38
8	KPF_6/g-C_3N_4	ethanol[e]	300 W Xe arc lamp	0.35 mM·h^{-1}	39
9	Nv-g-C_3N_4	ethanol[g]	250 W sodium lamp	1.30 mM·h^{-1}	40
10	g-C_3N_4 with N vacancies	ethanol[g]	250 W sodium lamp	2.00 mM·h^{-1}	41
11	g-C_3N_4 carbon	2-propanol[f]	300 W Xe lamp	0.38 mM·h^{-1}	42
12	oxygen-enriched g-C_3N_4	2-propanol[e]	300 W Xe lamp	1.20 mM·h^{-1}	43
13	g-C_3N_4-SiW_{11}	methanol[f]	300 W Xe lamp	0.30 mM·h^{-1}	44
14	KH_2PO_4/g-C_3N_4	ethanol[e]	300 W Xe arc lamp	0.75 mM·h^{-1}	45
15	g-C_3N_4-CoWO	organic electron donors	300 W Xe arc lamp	0.09 mM·h^{-1}	46
16	Au/g-C_3N_4	ethanol[e]	300 W Xe arc lamp	0.10 mM·h^{-1}	47
17	ACNN	2-propanol[e]	300 W Xe lamp	5.10 mM·h^{-1}	48
18	Ti_3C_2/g-C_3N_4	2-propanol[e]	300 W Xe lamp	0.11 mM·h^{-1}	49
19	BNQDs/UPCN	2-propanol[e]	300 W Xe lamp	0.07 mM·h^{-1}	50
20	AKMT/C_3N_4	ethanol[e]	300 W Xe lamp	1.37 mM·h^{-1}	51
21	*p*-TFAB-C_3N_4	ethanol[d]	24 W household LED	2.00 mM·h^{-1}	this work

[a]The reaction systems were exposed to lamps with main emission from 420 nm ($\lambda \geq 420$ nm). [b]$\lambda > 320$ nm. [c]Production rates were determined based on slopes of graphs in the initial time interval. [d]90 vol %. [e]10 vol %. [f]5 vol %. [g]0.789 g·L^{-1}.

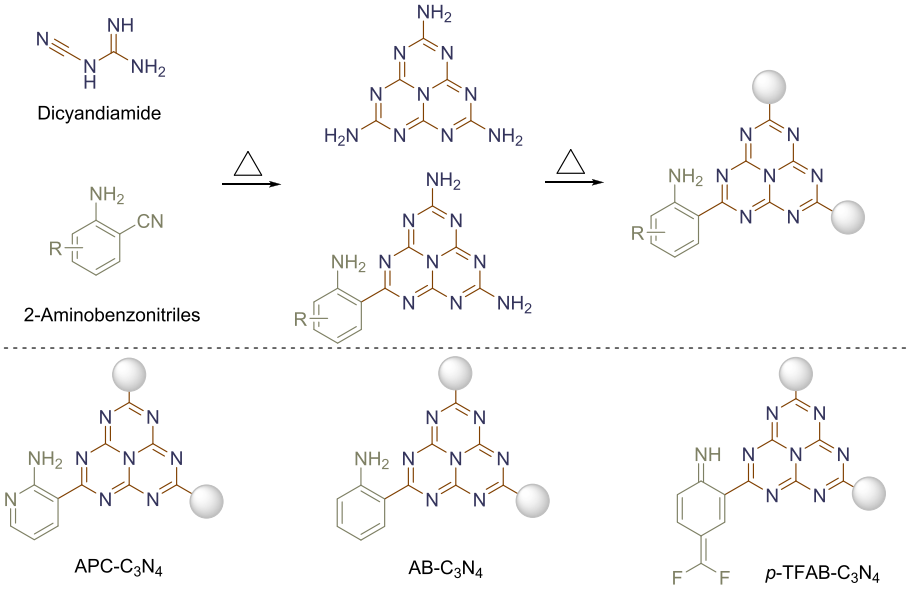

Figure 2. Synthesis of aryl amino PCNs.

$[Ru^{II}(Me_2phen)_3]^{2+}$ (Me_2phen = 4,7-dimethyl-1,10-phenanthroline) and $Ir(OH)_3$ (or cobalt catalyst).[19] In addition, Yerushalmi et al.[20] and Piao et al.[21] designed titanium oxide (TiO_2) doped with silicon or gold and Pt/TiO_2(anatase) for the production of H_2O_2 from water, respectively. Shiraishi's group reported on resorcinol-formaldehyde resins[22] for the production of H_2O_2 from water and O_2 under the irradiation of solar energy. PCN-based photocatalysts have also been used for the generation of H_2O_2. For example, Shiraishi's group described an excellent pyromellitic diimide (PDI)-modified PCN catalyst to generate 50.6 mmol of H_2O_2 in 48 h.[23] It should be noted that these excellent photocatalysts facilitated the production of H_2O_2 directly from water, but one drawback of this H_2O_2 generation process is to overcome high kinetic barriers, that, as a consequence, limits the amount of H_2O_2 production.[24,25] Alternatively, mixtures of water and alcohols such as ethanol have become highly attractive since ethanol can be obtained directly via the hydrolysis of biomass.[26] Teranishi et al. demonstrated that an Au-doped TiO_2 catalyst is appropriate,[24c] and, subsequently, Moon et al. revealed an excellent TiO_2 catalyst with reduced graphene oxide (rGO).[27] Parallelly, Yamashita and van Der Voort groups reported hydrophobic metal−organic frameworks and covalent organic frameworks

https://doi.org/10.1021/acscatal.1c03733
ACS Catal. XXXX, XXX, XXX−XXX

(COFs), respectively, for the generation of H_2O_2 from a mixture of water and alcohols.[28,29]

In addition to all of the abovementioned catalysts, PCNs were also used to produce H_2O_2 from mixtures of water and alcohols (Table 1). More specifically, PCNs in conjunction with transition-metal catalysts, nitrogen vacancies, mesoporous morphologies, oxygen enrichment, or alkali metal dopants, have shown excellent reactivity.[32−51] Notwithstanding all of these excellent photocatalysts, a high-power light source (at least >150 W) was essential to achieve high reactivity, and a higher production rate of the generated H_2O_2 was only possible with at least 250 W light power (very expensive lamps). From all of these data, it is clear that a robust catalyst is essential to reduce cost and increase production. Herein, we report on a difluoromethylene-substituted aryl amino PCN catalyst that reaches 2.0 mM·h^{-1} of H_2O_2 production with 24 W household LEDs and is stable for more than 30 h (Figure 1b). The apparent quantum yield (AQY) is 36.7% at 456 nm (see the Supporting Information). Compared to all of the existing protocols using PCNs, this robust heterogeneous catalyst based on LEDs produces a higher concentration of H_2O_2 at a similar rate. Furthermore, to gain a comprehensive knowledge of its action, we have characterized it with ^{1}H, ^{13}C, ^{15}N, and ^{19}F MAS solid-state NMR spectroscopy, Fourier transform infrared spectroscopy (FTIR), diffuse-reflectance UV/vis spectroscopy, Mott−Schottky plots, Brunauer−Emmett−Teller (BET) analysis, high-resolution transmission electron microscopy (HRTEM), and multiscale/level computational chemistry.

RESULTS AND DISCUSSION

Different aryl amino PCNs were synthesized by heating dicyandiamide (DCDA, 42 g) and the corresponding amino aryl nitriles (0.7 g, 1.6 wt %) in H_2O (160 mL) at 95 °C until the mixture was completely dried (Figure 2). The resulting mixture was removed, ground in an agate mortar, and loaded into a stainless steel chamber. Later, the chamber was heated to 585 °C in a GERO carbolite oven (type F70-200, power 1.5 kW) for 244 min under air. The temperature was maintained for 4 h followed by cooling the chamber to room temperature in 6 h.

After the synthesis of aryl amino PCNs, Fourier transform infrared spectra (FTIR) were collected using a Varian 610-IR FTIR spectrometer. The sample was analyzed in the range of 400−4000 cm^{-1} with 16 scans at a 4 cm^{-1} resolution. As shown in Figure 3, all of the stretching modes of the aromatic CN heterocycles around 1250−1600 cm^{-1} and the breathing mode of the triazine units at 800 cm^{-1} were observed. These signals clearly showed that the modification did not change the core of the polymeric structure of PCN and are similar to the pristine C_3N_4.[3a] Additionally, the Brunauer−Emmett−Teller (BET) specific surface area (S_{BET}) was determined from the low-temperature nitrogen adsorption/desorption isotherms and was ∼12 m^2·g^{-1} for *p*-TFAB-C_3N_4, which is higher than that for the bulk g-C_3N_4 (Figure S2).[23]

The band gaps of all of the aryl amino PCNs were determined from Tauc plots (ca. 2.8 eV), which were similar to the pristine C_3N_4 (Figure S4). Mott−Schottky experiments were also performed for the determination of flat band potentials (E_{fb}). The positive slope of the Mott−Schottky curve indicated the n-type nature of the aryl amino PCNs. Based on the intersection between the Mott−Schottky plot and the baseline, E_{fb} of aryl amino PCNs was approximately −0.69 V vs RHE. It is generally considered that the bottom potential of the conduction band (CB) for an n-type semiconductor is ∼0.2 V more negative than

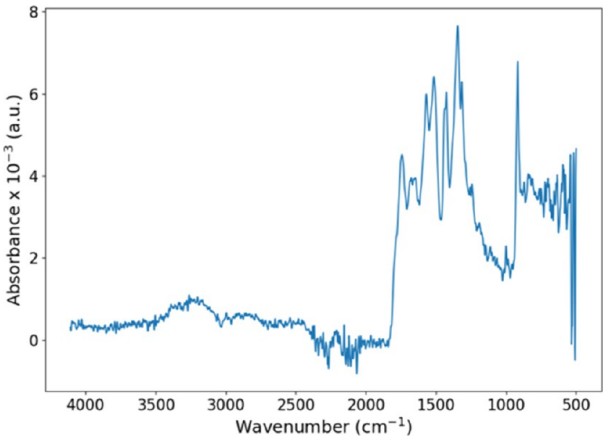

Figure 3. FTIR spectrum of *p*-TFAB-C_3N_4.

E_{fb}. Therefore, the CB of aryl amino PCNs was ca. −0.89 V vs RHE and the valence band (VB) was 1.97 V vs RHE (Figures S5 and S6).

To further obtain the structural information of aryl amino PCNs, solid-state MAS NMR was performed (Figure 4). To the best of our knowledge, high-resolution ^{1}H MAS NMR spectra of this type of material have not been reported before. The ^{1}H MAS NMR spectrum of *p*-TFAB-C_3N_4 revealed two main signals: (i) one from >NH linkers at 8.9 ppm and (ii) another from −NH_2 terminal groups at 4.2 ppm. The high signal intensity from the >NH linkers in comparison to the low signal integral of the −NH_2 terminal groups (fitted ratio of ∼0.8:0.2) reflected the high degree of polymerization among the melem monomers in the network. The two observed ^{13}C resonances originated from the "edge" (C_e; 165 ppm shift) and the "internal" (C_i; 157 ppm) carbon sites, as depicted in Figure 4b. The signal of C_e was expected to have a higher intensity than C_i as a consequence of closer distances to protons of the >NH and −NH_2 groups, which enabled more efficient cross-polarization in the CPMAS experiment. This is in agreement with previously reported ^{1}H−^{13}C CPMAS spectra of g-C_3N_4.[3d,52] Noteworthy, the ^{13}C spectrum of the *p*-TFAB-C_3N_4 sample revealed an additional partially resolved signal at 163 ppm, which had not been observed before. As this resonance originated from the carbon atoms adjacent to the >NH linkers, this indicated distinct network arrangements in the sample compared to the previous reports.

No other carbon signals from either the aromatic or nonaromatic species were observed in the ^{1}H−^{13}C CPMAS spectrum. However, the ^{1}H−^{15}N CPMAS spectrum revealed all of the expected nitrogen resonances for the g-C_3N_4 structure being composed of melem monomeric units. The signals at −188 and −225 ppm correspond to the nitrogen atoms embedded at the edge (N_e) and inside (N_i) of the monomer units. The N_e/N_i signal intensity ratio was higher than the expected 6:1 because N_i was situated at a farther distance from the closest protons, which made cross-polarization less efficient for this nitrogen site. The intensities of both the signals increased when the contact time in the CPMAS experiment was increased from 2 to 4 ms, which corroborated signal assignments. The resonances at −244 and approximately −264 ppm originated from linkers (>NH) and terminal −NH_2 groups, respectively. It is worth noting that the signal of the −NH_2 groups is over-represented in the ^{1}H−^{15}N CPMAS spectrum since there are

https://doi.org/10.1021/acscatal.1c03733
ACS Catal. XXXX, XXX, XXX−XXX

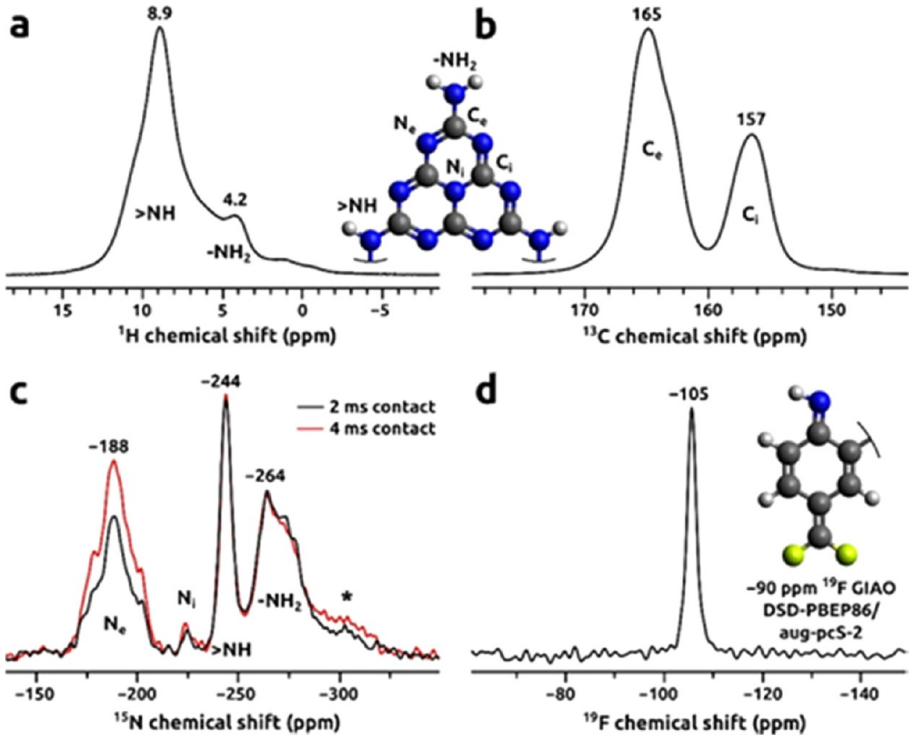

Figure 4. ^{1}H MAS NMR, $^{1}H-^{13}C$, ^{19}F, and $^{1}H-^{15}N$ CPMAS spectra of the *p*-TFAB-C_3N_4 sample.

two available protons to cross-polarize compared to the >NH moiety. These signal assignments are in pair with the previous NMR study on $^{13}C/^{15}N$-isotope-enriched g-C_3N_4 and with theoretical predictions of $^{13}C/^{15}N$ NMR shifts in g-C_3N_4 by density functional theory (DFT).[52,53] The ^{19}F MAS NMR spectrum revealed a single resonance and consequently confirmed the successful incorporation of the fluorine atoms at a sole chemical site. The ^{19}F chemical shift of −105 ppm suggests the presence of the $=CF_2$ moiety,[54,55] and it was corroborated further by quantum chemical calculations. The ^{19}F chemical shift calculations at the robust DSD-PBEP86/aug-pcS-2 level of theory[56] for the model of difluoromethylene functionality shown in Figure 4d (see SI for details) resulted in chemical shift prediction of −90 ppm, which is close to the experimental results given the wide chemical shift range of the ^{19}F nucleus. Hence, we conclude that our combined NMR/DFT characterization confirms the proposed chemical model of the catalyst.

After achieving all of the characterizations of the aryl amino PCNs, we were then interested in observing their catalytic potential for the generation of H_2O_2 from a mixture of water and ethanol (Table 2). To our delight, initial evaluation of the photocatalytic performance from the (1:1, v/v) mixture of water and ethanol generated up to 1.2 mM of H_2O_2 within 1 h with *p*-TFAB-C_3N_4. In general, the higher the concentration of ethanol in the mixture, the higher the contact possibility of ethanol and the available active sites, which leads to better yield of H_2O_2. However, water can also increase the selectivity of H_2O_2 due to the hydration between H_2O_2 and the water molecule.[32] Later, careful optimizations led to the best ethanol/water ratio as 9:1. Furthermore, the presence of an acid was essential because it can prevent the decomposition of H_2O_2 under long reaction time and high concentration of formed H_2O_2 conditions. Indeed, it

Table 2. Generation of H_2O_2 from Water and Ethanol Mixture Using Aryl Amino PCNs under the Irradiation of Blue LEDs

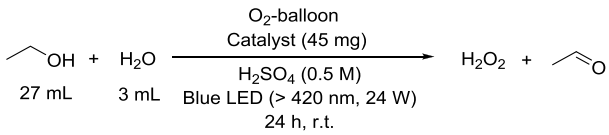

entry	catalyst	H_2O_2 (mM)[a]
1	APC-C_3N_4	15.89
2	AB-C_3N_4	24.44
3	*p*-TFAB-C_3N_4	25.64
4	g-C_3N_4	14.05

[a]Concentrations were determined by redox titration with $KMnO_4$ and the results were the average value of two experiments under the same reaction conditions.

was found that 0.5 M of H_2SO_4 was an ideal choice for this stabilization. In addition, O_2 and a light source were essential to trigger the reaction, and without them, no formation of H_2O_2 was observed. The evaluation of all of the optimization reactions led us to these optimal conditions (for detailed optimization studies, see Table S1): a mixture of ethanol (27 mL), H_2O (3 mL), and H_2SO_4 (0.5 M) containing the catalysts (45 mg) was irradiated under blue LED (>420 nm, 24 W) at room temperature under O_2 saturation conditions. After achieving 25.64 mM H_2O_2 in 30 h, *p*-TFAB-C_3N_4 catalyst was recollected by centrifugation and reutilized for further reactions. Indeed, this catalyst was successfully recycled at least four times (Tables S8 and S9).

To further analyze the stability of the catalyst (***p*-TFAB-C_3N_4**) from Table 2, TEM studies on the catalyst before and after the reaction were performed (Figure 5). TEM and

https://doi.org/10.1021/acscatal.1c03733
ACS Catal. XXXX, XXX, XXX−XXX

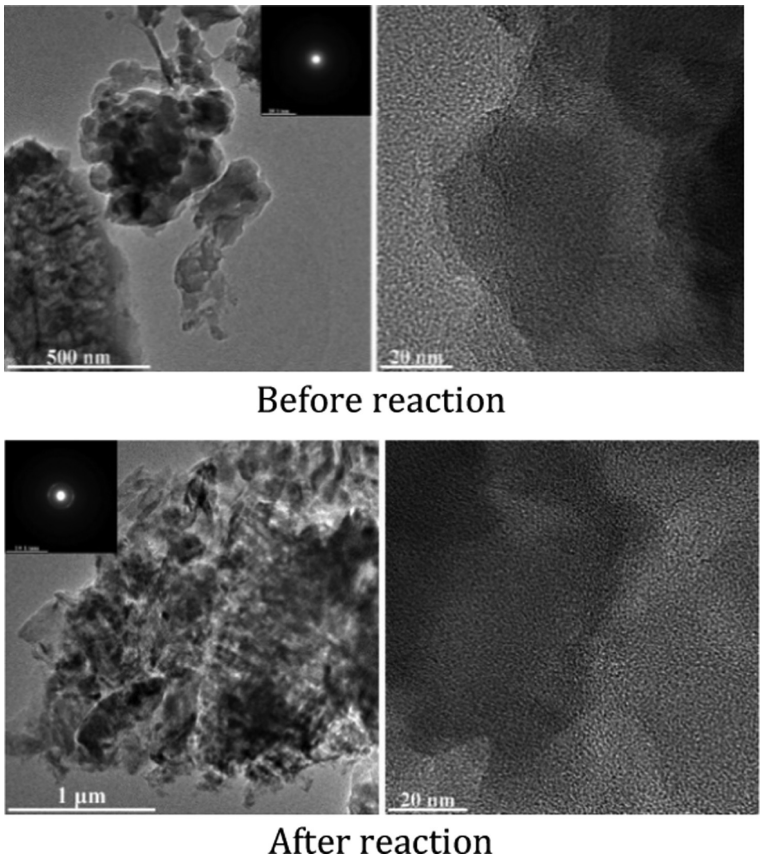

Figure 5. TEM and HRTEM images of *p*-TFAB-C_3N_4 before and after the reaction. TEM image and selected-area electron diffraction pattern (SAED) of PCN were recorded by JEOF-2100F.

HRTEM images of *p*-TFAB-C_3N_4 (before reaction) revealed a two-dimensional structure, i.e., the nanoflake structure with an amorphous phase (embedded SAED pattern). Even though the low-magnification TEM image of PCN after the reaction showed a denser and thicker morphology, HRTEM showed the same nanoflake microstructure at the edge. As a result, the difference in the morphology was attributed to the observed thickness of particles, and it can be concluded that the reaction did not change the microstructure of the PCN, indicating a high stability during the reaction conditions. This clearly suggested excellent recyclability of the *p*-TFAB-C_3N_4 catalyst under the reaction conditions (Figures S8 and S9).

To experimentally analyze the kinetics of the photocatalytic H_2O_2 generation, concentrations of the formed H_2O_2 and the decomposition of H_2O_2 under the irradiation of blue LEDs were measured. As shown in Figure 6, concentrations of the formed H_2O_2 with various aryl amino PCNs were increased linearly within 8 h and accumulated slowly over time. Parallel to this, decomposition of H_2O_2 was also investigated and H_2O_2 was decomposed dramatically when its concentration was very high. All of the aryl amino PCNs showed no obvious difference in the decomposition rate. It is worth noting that the decay rate of H_2O_2 was much slower in the presence of the acid compared to its absence. Therefore, we assumed that the formation and decomposition of H_2O_2 are in accordance with the zero-order and first-order reaction kinetics, respectively.

Finally, to disclose the mechanism of this reaction, the $^{18}O_2$-labeling experiment was carried out to investigate the oxygen source of the formed H_2O_2. The generated hydrogen peroxide from the mixture of O_2 gas ($^{16}O_2$) and labeled molecular oxygen ($^{18}O_2$) was subsequently made to react with PPh_3 and concomitantly analyzed by GCMS. As shown in Figure 7, the mixture of phosphine oxides ($^{16}O = PPh_3$ and $^{18}O = PPh_3$) was observed, which clearly proved that the oxygen source of the formed H_2O_2 was the O_2 gas.

To further investigate the performance of the photogenerated carrier transfer rate of the catalysts, electrochemical impedance spectroscopy (EIS) measurements were carried out. As shown in Figure 8, following the Nyquist plots, the diameter of each of the semicircle was related to the charge transfer resistance at the electrode surface of the catalyst. Therefore, the smaller the diameter, the faster the charge transfer and better the charge separation. Compared to the bare electrode, resistances at the electrode surfaces with the aryl amino PCNs were all smaller and *p*-TFAB-C_3N_4 had the smallest resistance. It should also be clearly noted that all of these aryl amino PCNs exhibited smaller resistance compared to the g-C_3N_4 catalyst that suggests that these aryl amino PCNs have slower recombination of the photogenerated electron−hole pairs. Additionally, the electrode with *p*-TFAB-C_3N_4 was also investigated under the O_2 and N_2 atmosphere in the presence and absence of light, respectively. It was obvious that *p*-TFAB-C_3N_4 under the O_2 atmosphere in the presence of light exhibited much smaller resistance compared to that of the N_2 atmosphere. The photogenerated electrons were consumed at the surface of the photocatalyst after reduction by

https://doi.org/10.1021/acscatal.1c03733
ACS Catal. XXXX, XXX, XXX−XXX

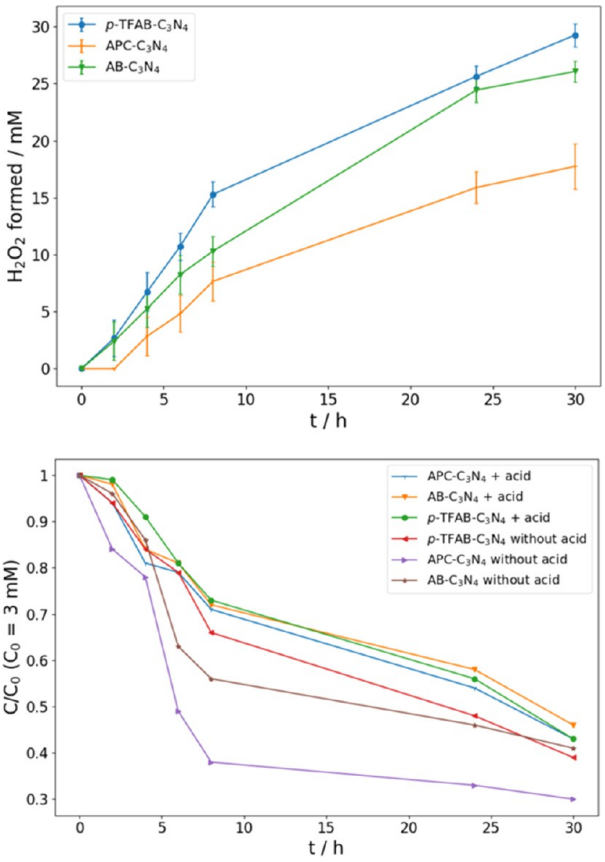

Figure 6. Photocatalytic H_2O_2 generation (top) and decomposition (down) with aryl amino PCNs under visible light. Concentrations were determined by redox titration with $KMnO_4$.

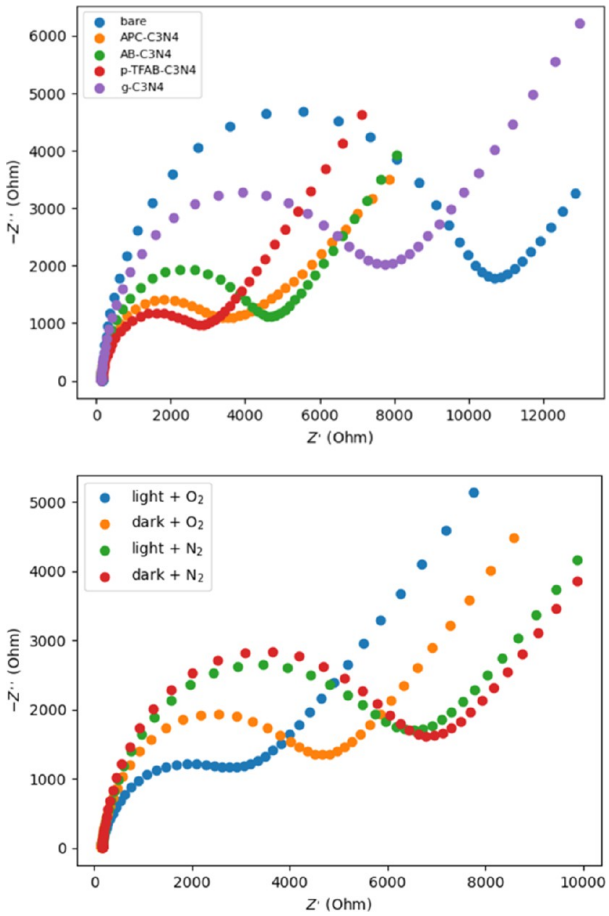

Figure 8. Electrochemical impedance spectroscopy Nyquist plots of various modified catalysts under air (top). Nyquist plots of *p*-TFAB-C_3N_4 under saturated N_2 or O_2 atmosphere (bottom). The measurements were performed in 80 μL of the solution containing 1 mM $K_3Fe(CN)_6$, 1 mM $K_4Fe(CN)_6$, and 150 mM NaCl. As a reference, one measurement was done on a bare working electrode.

O_2, which indicated that O_2 facilitated charge separation and prevented recombination of photoinduced charges and holes.

Furthermore, to identify the possible radicals involved in this reaction, ESR analysis with 5,5-dimethyl-1-pyrroline *N*-oxide (DMPO) as a spin trapping reagent was carried out (Figure 9). The ESR spectra of an *in situ* photoreaction of *p*-TFAB-C_3N_4/EtOH/O_2 with the DMPO system indicated that four radicals could be identified in this photocatalytic system: (1) DMPO−$^{\bullet}$OOH; (2) radical of the catalyst; (3) DMPO−$^{\bullet}$OEt; and (4) nitroxide degradation product of DMPO.[57] From the below table, parameters of the radical of the catalyst and DMPO−$^{\bullet}$OOH adduct were similar to the references.[58,59]

Therefore, we suggest that oxygen was reduced via one-electron reduction due to the strong signal of the DMPO−$^{\bullet}$OOH adduct. The signals of the DMPO−$^{\bullet}$OEt adduct and nitroxide degradation radical of DMPO were weak and overlapped with the DMPO−$^{\bullet}$OOH adduct signal. It is also worth noting that each of these reaction components played a crucial role for the generation of $^{\bullet}$OOH radical (Table S2).

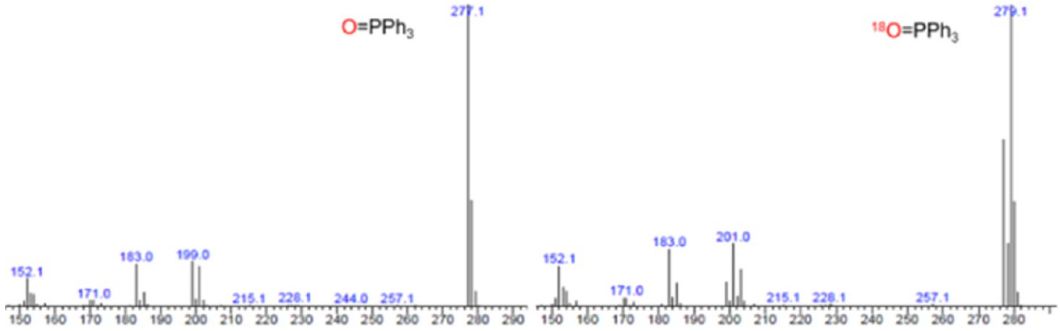

Figure 7. Mass spectra for the labeling reaction.

https://doi.org/10.1021/acscatal.1c03733
ACS Catal. XXXX, XXX, XXX−XXX

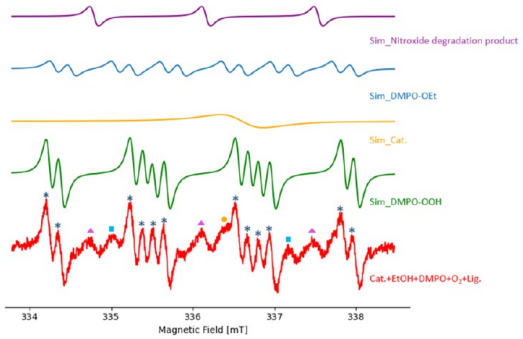

Radical	A_N [mT]	A_H [MT]	g_{iso}	Ref.
p-TFAB-C_3N_4	-	-	2.0038	This work
g-C_3N_4	-	-	2.0034	[3d]
DMPO-•OOH	1.30	1.03 (1H) 0.15 (1H)	2.0066	This work
DMPO-•OOH	1.31	1.03 (1H) 0.14 (1H)	2.0061	[58]
DMPO-•OEt	1.35	0.76 (1H) 0.21 (1H)	2.0065	This work
DMPO-•OEt	1.35	0.74 (1H) 0.17 (1H)	-	[59]

Figure 9. ESR spectra measured at room temperature for the reaction solution in the presence of a 200 mW solid-state laser (447 nm). The EPR spectra was simulated with Matlab2018b using the EasySpin-6.0 module.

These data agree with the representative supramolecular models designed to disclose, computationally, possible reaction mechanisms and locations of the various species in relation to the catalysts. The main focus was on the edge regions of the nanoflakes where the functional group was attached. In the initial configurations of the reduction dynamics, the O_2 molecules were surrounded by the solvent, located far apart from one another and relatively close to the catalyst interfaces. After a few picoseconds of RMD, most of the O_2 reached the catalyst regions where the NH or NH_2 groups were located, stabilizing their position there through intermolecular hydrogen-bonding interactions. This is seen in Figure 10, where the O_2 maximum density maps, rendered as red contours, are superimposed to the molecular structures of the two catalysts (solvent molecules are also displayed as sticks).

The extension of these areas gives an idea of the motion of the oxygen near the interface, which is, apparently, very limited. This is in contrast with its high mobility in solution where the density contours are more extended. It can also be noticed that the connections of the oxygens are sometimes reinforced by the cooperative action of various amine moieties close by and, when the *p*-TFAB fragment is present, by a relatively strong interaction with its nitrogen group (Figure 11).

A consequence of these local constraints on O_2 is a sort of entrapment that induces a relocation of the surrounding solvent molecules. Practically, both ethanol and water adopted a more favorable orientation to interact/react with O_2. It is worth mentioning that the interfacial behavior of the solvent is similar for the two catalysts. Indeed, the RDF plots shown in Figure 12 confirm the tendency of ethanol to exchange/release its H(OH) with/to the amine nitrogen or nonprotonated nitrogens of both catalysts and to reorient its other hydrogens toward the π density of the rings (peak centered at 2 Å in the carbon RDF plot). The *p*-TFAB functionalization represents another active O_2 binding location at the catalyst edges that could be strengthened by self-assembly of the graphitic-like sheets in T-shaped or parallel orientations (Figures 11 and 12).

A more straightforward characterization of the O_2 reduction mechanism, in general terms, was obtained through the examination of the atom−atom distance distribution functions of O_2 with both nitrogen and carbon sites of the catalysts and with the hydrogens of catalysts and the solvent (Figure S10). The first RDFs confirm again that the mechanism starts with the connection of O_2 to the N sites through H-bond interactions (peak at 3.2 Å—red curve) and that the main actor is ethanol, which releases its H(OH) to both or one of the oxygen atoms (red peak at about 1 Å in both a and b plots—right-hand side). However, the presence of the first peak at short distances (about 1.1 Å in the b plot) ascribed to the catalyst suggests that *p*-TFAB plays a role in the reduction process by providing the oxygen with the hydrogen that in the other case (nonfunctionalized melem) was released by water. The most striking effect of these interactions is an increase in H_2O_2 production, which is evident in the trend displayed in Figure 13.

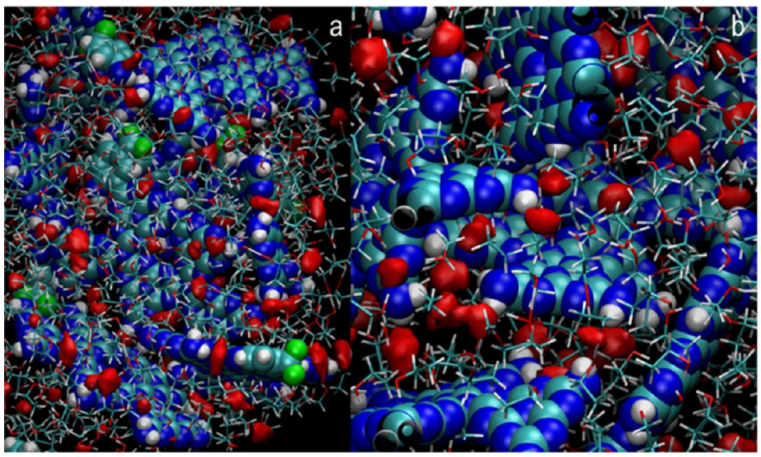

Figure 10. Simulation snapshots of the complex models comprising the catalyst (a) with *p*-TFAB and (b) without it (vdW spheres), ethanol and water molecules (sticks), and red high-density contours identifying the O_2 molecules. Color code: C, cyan; O, red; N, blue; F, green; H, white.

https://doi.org/10.1021/acscatal.1c03733
ACS Catal. XXXX, XXX, XXX−XXX

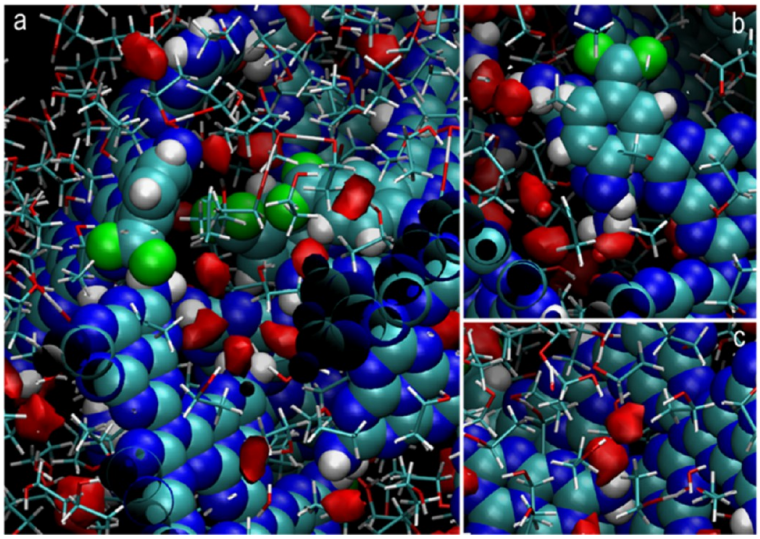

Figure 11. Catalysts with *p*-TFAB (vdW spheres), ethanol and water molecules (sticks), and red high-density contours identifying the O_2 molecules. Color code: C, cyan; O, red; N, blue; F, green; H, white. (a) Self-assembly of the various catalyst units and entrapment of the O_2 molecules interacting with the NH_2 groups. (b) One of the *p*-TFAB groups. (c) Capture of the O_2 molecules inside the pores of the material.

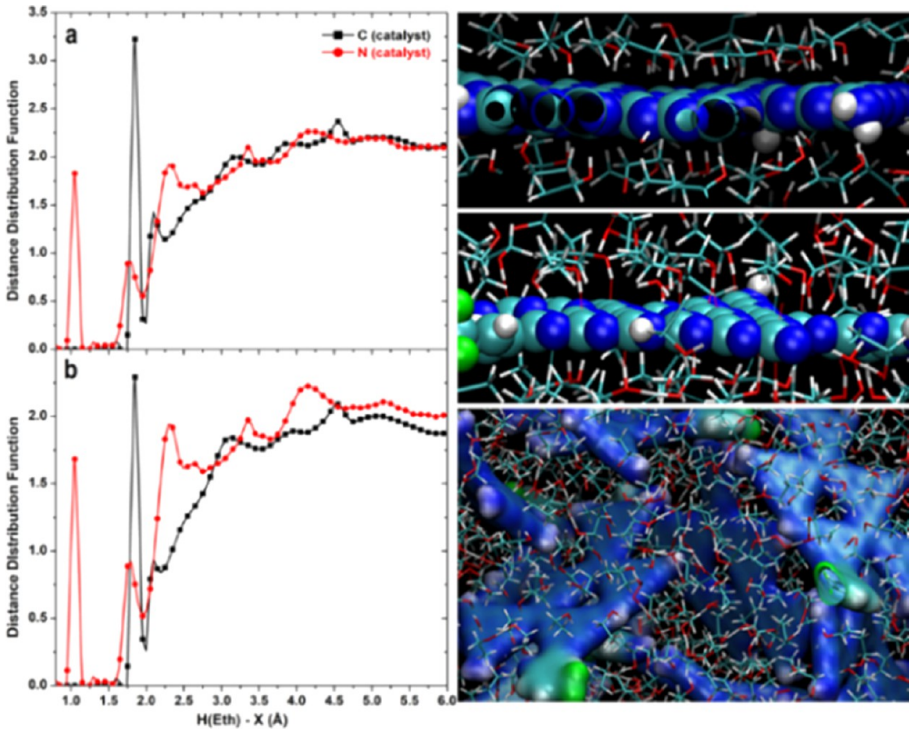

Figure 12. Ethanol hydrogens−C/N atoms of the catalyst distance distribution functions for (a) nonfunctionalized and (b) *p*-TFAB functionalized systems. On the right-hand side, the molecular models depict the orientation of the ethanol molecules (sticks) in relation to the two supports (vdW or accessible surface representations). The red dashed lines indicate the coordination of the OH groups to the interface.

As far as the reaction mechanism is concerned, two possible reaction models were identified, which are shown in Figure 14. The observed phenomena were not induced by specific biases and happened spontaneously, suggesting that, in the presence of the catalysts, the energy barriers could be overcome at the simulated temperature. For both reaction models, it is apparent that a critical step is the restraint of the O_2 mobility by its hydrogen bonding to an edge NH or NH_2 group of the catalyst. This induces an ad hoc rearrangement of O_2 relative to the surrounding solvent species that start to reorient their active hydrogens toward each of the oxygens. As displayed in Figure 14A (path a), the hydrogens released to the O_2 molecule come from ethanol. Another possible pathway observed during the simulation was the one where the NH group of the catalyst functioned both as mediator and proton donor (Figure 14B, path b). Indeed, the NH or NH_2 of the linker is initially

https://doi.org/10.1021/acscatal.1c03733
ACS Catal. XXXX, XXX, XXX−XXX

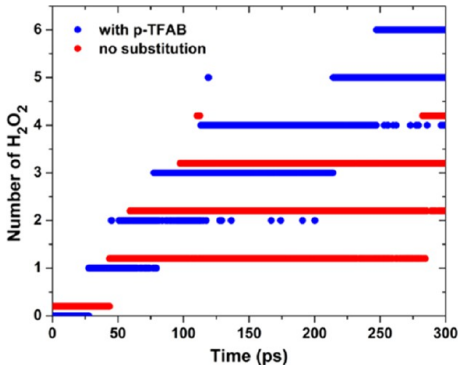

Figure 13. Evolution of the number of H_2O_2 produced during the RMD for the functionalized and nonfunctionalized supports.

protonated and thus prone to give a hydrogen atom to O_2, which almost simultaneously receives another H from the ethanol adjacent to the other O (Figure S12). During the RMD simulations, we could not observe the formation of acetaldehyde, which is the main ethanol photooxidation product because all of the effects of visible light were not included in the models. Thus, we resorted to QC nudged elastic band (NEB) calculations on representative models of the catalysts (Figure S13) interacting with just an O_2 and an ethanol molecule to reproduce the whole reaction mechanisms at the edges of the materials and to estimate the energy barriers involved in these processes (Figure 15).

The initial action is a sort of immobilization of O_2 via hydrogen-bonding interactions with the −NH or $-NH_2$ group of the catalyst and the ethanol OH moiety (left panels in Figure 15 corresponding to reactant configuration). The transition state (TS in Figure 15) consists of the same OOH* intermediate obtained after the ethanol H(OH) migration on O_2 and, in the case of the incorporation of *p*-TFAB, in the addition of an H (from the CH_2 of ethanol) to the *p*-TFAB NH moiety. The final stabilization is achieved by a simultaneous hydrogen transfer from $-NH_2$ of the catalysts (and CH_2 of ethanol in pristine melem) and the formation of H_2O_2 and acetaldehyde (right panels in Figure 15, corresponding to product configurations). The activation energies are approximately 28 and 23 kcal·mol^{-1} for path a and path b, respectively. Obviously, path b showed lower activation energy, which is also consistent with our experimental results. However, it should be noted that catalysts were protonated by $-H(CH_2)$, which was not the favorable step compared to H(OH). However, due to the instability of the $CH_3CH_2O\cdot$ radical, $-H(CH_2)$ was used to estimate the activation energy and the real activation energy is probably even less. Therefore, we propose the catalysts act as both proton donors and mediators. In addition, after aligning the energy of the reaction products, it is apparent that in the *p*-TFAB-doped system, the reagents are stabilized by about 16 kcal·mol^{-1}, which can suggest the tendency to more favorable interactions between the O_2/ethanol mixture with the *p*-TFAB termination.

Furthermore, to disclose the effects of light on the doped catalyst, we used the time-dependent extension of DFT (TDDFT) at the B3LYP/6-31G(d) level of theory, in line with Shiraishi and co-workers,[23] and simulated the UV/vis spectrum of the *p*-TFAB-doped system. An intense absorption peak located at about 423 nm was identified (Figure S14) with its corresponding structure (see the Supporting Information). In line with previous observations,[23,32] in the excited-state conformation, the hydrogen of *p*-TFAB is connected to the nearby nitrogen of the g-C_3N_4 unit, suggesting and confirming (in agreement with the RMD simulations) that the *p*-TFAB nitrogen is available for active hydrogen exchanges and thus a very efficient site in the H_2O_2 production mechanism.

Based on all of the above information, we propose the mechanism of this reaction and robustness in the presence of the aryl amino PCNs (Figure 16). Before the irradiation of light, the amino group NH of the *p*-TFAB fragment reinforced the interaction with O_2 through hydrogen bonding. This restrained O_2 mobility and facilitated the ad hoc rearrangement of ethanol surrounded by O_2 (**Step 1**). The NH linker was further protonated by H(OH) in ethanol, which was close to the NH linker (**2**). Upon photocatalyst activation by the blue LED, formation of photogenerated electrons and holes occurred and consequently, ethanol as an electron donor was oxidized.[5e] At the same time, O_2 was reduced by the catalyst to form the superoxide radical anion via one-electron reduction (**Step 2**). Based on NEB calculations, H(NH) is more favorable than H(OH) to be deprotonated by superoxide radical anions (**3** and **4**). After protonation of the superoxide radical anion, acetaldehyde and hydroperoxide radicals were formed, which were verified by ESR and catalyst **1** was regenerated (**Step 3**). Finally, generation of H_2O_2 occurred in the final step (**Step 4**) by abstracting the hydrogen atom radical and forming acetaldehyde.

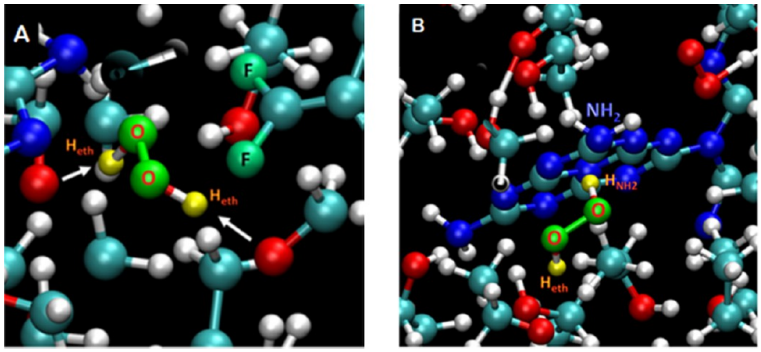

Figure 14. Two distinct reaction models where the hydrogens of the final product (H_2O_2) come from (a) ethanol and (b) NH group of the catalyst and ethanol. O_2 and H_2O_2 are green and the released hydrogens are yellow.

https://doi.org/10.1021/acscatal.1c03733
ACS Catal. XXXX, XXX, XXX−XXX

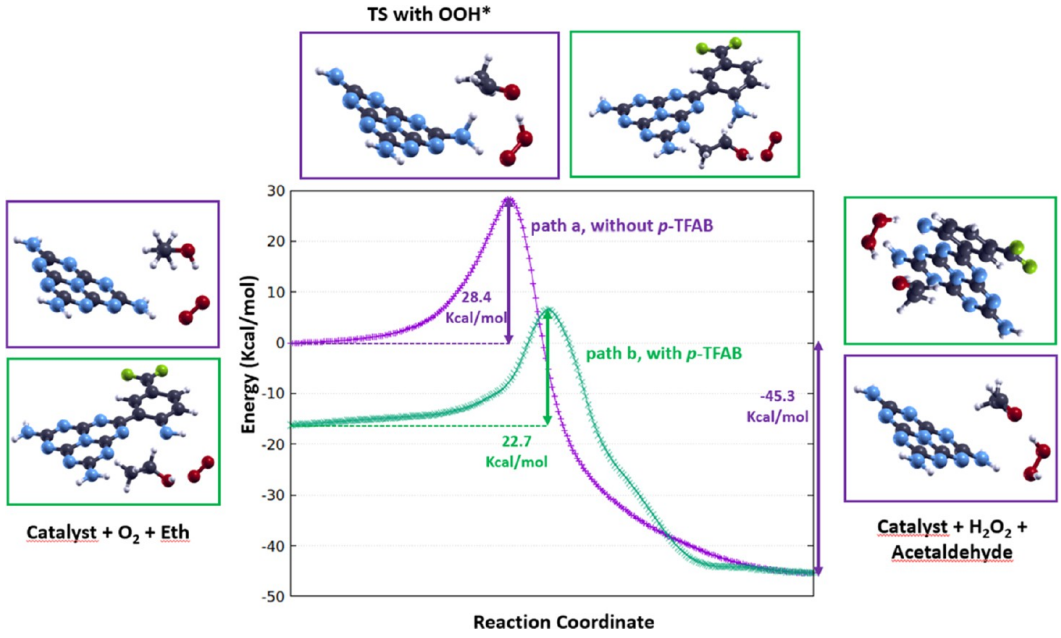

Figure 15. NEB simulations of the H_2O_2 generation process for two pathways. Hydrogens of the final product (H_2O_2) come from ethanol (path a, purple) or from the NH group of the catalyst and ethanol (path b, green). C, N, O, H, and F atoms are dark gray, blue, red, white, and green, respectively.

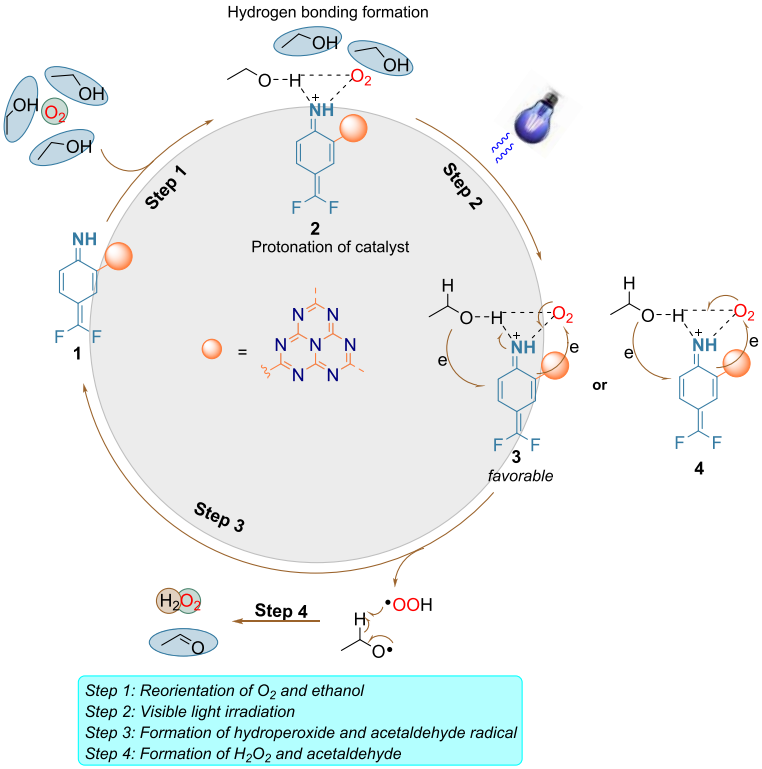

Figure 16. Proposed mechanism for photocatalytic H_2O_2 formation.

CONCLUSIONS

In conclusion, we constructed an effective photocatalytic system for the production of H_2O_2 in the presence of household LEDs. The novel aryl amino PCNs with more negative CB promoted faster O_2 reduction and facilitated higher concentration of H_2O_2. It is also worth noting that the aryl amino PCNs exhibited smaller resistance at the surface of the photocatalyst, which suppressed the recombination of the photoinduced electrons and holes. Our work provides higher concentration of H_2O_2 (25.64 mM), which demonstrates that the modification with aryl

https://doi.org/10.1021/acscatal.1c03733
ACS Catal. XXXX, XXX, XXX−XXX

amino moiety is a promising method to enhance the photocatalytic performance of H_2O_2 generation and facilitate O_2 reduction. The critical advancement of this work is the synthesis of an efficient H_2O_2 generation photocatalyst and its atomic-level understanding by combined ^{19}F, ^{13}C, ^{1}H, and ^{15}N solid-state MAS NMR at natural abundance. This methodology reveals that the chemical structure of the semiconducting PCNs contains both NH linkers, $-NH_2$ terminal groups, and difluoromethylene functional groups. Our study emphasizes the importance of solid-state NMR spectroscopy for the elucidation of structure−property relationships and is generally applicable to all of the PCN-related materials. In addition, with the help of computational studies, we disclosed the possible reaction model in the atomic level, which provided a new sight for the modification of photocatalysts for photocatalytic H_2O_2 production.

■ ASSOCIATED CONTENT

Supporting Information

The Supporting Information is available free of charge at https://pubs.acs.org/doi/10.1021/acscatal.1c03733.

BET analysis, details of reaction setup and equipment, optimization of reaction conditions, EIS measurements, analysis of electronic energy levels, solid-state NMR analysis, ESR measurements, and detailed information of computational chemistry including molecular dynamics simulations and QC calculations (PDF)

■ AUTHOR INFORMATION

Corresponding Author

Shoubhik Das − *Department of Chemistry, Universiteit Antwerpen, 2020 Antwerpen, Belgium;* orcid.org/0000-0002-4577-438X; Email: shoubhik.das@uantwerpen.be

Authors

Tong Zhang − *Department of Chemistry, Universiteit Antwerpen, 2020 Antwerpen, Belgium*

Waldemar Schilling − *Department of Chemistry, Universiteit Antwerpen, 2020 Antwerpen, Belgium*

Shahid Ullah Khan − *Department of Bioscience Engineering, Universiteit Antwerpen, 2020 Antwerpen, Belgium*

H. Y. Vincent Ching − *University of Antwerp, BIMEF, 2610 Wilrijk, Belgium*

Can Lu − *Department of Materials and Environmental Chemistry, Stockholm University, 10691 Stockholm, Sweden*

Jianhong Chen − *Department of Materials and Environmental Chemistry, Stockholm University, 10691 Stockholm, Sweden*

Aleksander Jaworski − *Department of Materials and Environmental Chemistry, Stockholm University, 10691 Stockholm, Sweden;* orcid.org/0000-0002-7156-559X

Giovanni Barcaro − *CNR-IPCF—Institute for Chemical and Physical Processes, 56124 Pisa, Italy*

Susanna Monti − *CNR-ICCOM—Institute of Chemistry of Organometallic Compounds, 56124 Pisa, Italy;* orcid.org/0000-0002-3419-7118

Karolien De Wael − *Department of Bioscience Engineering, Universiteit Antwerpen, 2020 Antwerpen, Belgium;* orcid.org/0000-0003-4495-0748

Adam Slabon − *Department of Materials and Environmental Chemistry, Stockholm University, 10691 Stockholm, Sweden;* orcid.org/0000-0002-4452-1831

Complete contact information is available at: https://pubs.acs.org/10.1021/acscatal.1c03733

Author Contributions

All authors have given approval to the final version of the manuscript.

Notes

The authors declare no competing financial interest.

■ ACKNOWLEDGMENTS

The authors acknowledge the Francqui foundation (Francqui lecturer award to S.D.) and the FWO Ph.D. Fellowship (to T.Z.) for the financial support. A.S. thanks the Swedish Energy Agency for financial support (Project No. 5050-1). S.U.K. and K.D.W. acknowledge FWO and ERANET-RUSPLUS Plasmonelectro-light. The authors also thank Dr. Tetyana Budnyak and Dr. Gandhi Sivaraman for fruitful discussions.

■ REFERENCES

(1) (a) Maeda, K.; Teramura, K.; Lu, D.; Takata, T.; Saito, N.; Inoue, Y.; Domen, K. Photocatalyst releasing hydrogen from water. *Nature* **2006**, *440*, No. 295. (b) Kudo, A.; Miseki, Y. Heterogeneous photocatalyst materials for water splitting. *Chem. Soc. Rev.* **2009**, *38*, 253−278. (c) Walter, M. G.; Warren, E. L.; McKone, J. R.; Boettcher, S. W.; Mi, Q.; Santori, E. A.; Lewis, N. S. Solar water splitting cells. *Chem. Rev.* **2010**, *110*, 6446−6473.

(2) (a) Calle-Vallejo, F.; Tymoczko, J.; Colic, V.; Vu, Q. H.; Pohl, M. D.; Morgenstern, K.; Loffreda, D.; Sautet, P.; Schuhmann, W.; Albiter Bandarenka, A. S. Finding optimal surface sites on heterogeneous catalysts by counting nearest neighbors. *Science* **2015**, *350*, 185−189. (b) Van Santen, R. A. Complementary Structure Sensitive and Insensitive Catalytic Relationships. *Acc. Chem. Res.* **2009**, *42*, 57−66. (c) Lee, I.; Delbecq, F.; Morales, R. M. A.; Zaera, F.; et al. Tuning selectivity in catalysis by controlling particle shape. *Nat. Mater.* **2009**, *8*, 132−138. (d) Stamenkovic, V. R.; Fowler, B.; Mun, B. S.; Wang, G.; Ross, P. N.; Lucas, C. A.; Marković, N. M. Improved Oxygen Reduction Activity on Pt3Ni(111) via Increased Surface Site Availability. *Science* **2007**, *315*, 493−497. (e) Behrens, M.; Studt, F.; Kasatkin, I.; Kühl, S.; Hävecker, M.; Pedersen, F. A.; Zander, S.; Girgsdies, F.; Kurr, P.; Kniep, B.-L.; Tovar, M.; Fischer, R. W.; Nørskov, J. K.; Schlögl, R. The Active Site of Methanol Synthesis over Cu/ZnO/Al2O3 Industrial Catalysts. *Science* **2012**, *336*, 893−897.

(3) (a) Wang, X.; Maeda, K.; Thomas, A.; Takanabe, K.; Xin, G.; Carlsson, J. M.; Domen; Antonietti, K. M. A metal-free polymeric photocatalyst for hydrogen production from water under visible light. *Nat. Mater.* **2009**, *8*, 76−80. (b) Maeda, K.; Wang, X. C.; Nishihara, Y.; Lu, D. L.; Antonietti, M.; Domen, K. Photocatalytic Activities of Graphitic Carbon Nitride Powder for Water Reduction and Oxidation under Visible Light. *J. Phys. Chem. C* **2009**, *113*, 4940−4947. (c) Zhang, J. S.; Sun, J. H.; Maeda, K.; Domen, K.; Liu, P.; Antonietti, M.; Fu, X. Z.; Wang, X. C. Sulfur-mediated synthesis of carbon nitride: Band-gap engineering and improved functions for photocatalysis. *Energy Environ. Sci.* **2011**, *4*, 675−678. (d) Zhang, J.; Zhang, G.; Chen, X.; Lin, S.; Mçhlmann, L.; Dołęga, G.; Lipner, G.; Antonietti, M.; Blechert, S.; Wang, X. C. Co-Monomer Control of Carbon Nitride Semiconductors to Optimize Hydrogen Evolution with Visible Light. *Angew. Chem., Int. Ed.* **2012**, *51*, 3183−3187.

(4) (a) Giusto, P.; Arazoe, H.; Cruz, D.; Lova, P.; Heil, T.; Aida, T.; Antonietti, M. Boron Carbon Nitride Thin Films: From Disordered to Ordered Conjugated Ternary Materials. *J. Am. Chem. Soc.* **2020**, *142*, 20883−20891. (b) Giusto, P.; Kumru, B.; Zhang, J.; Rothe, R.; Antonietti, M. Let a Hundred Polymers Bloom: Tunable Wetting of Photografted Polymer-Carbon Nitride Surfaces. *Chem. Mater.* **2020**, *32*, 7284−7291. (c) Giusto, P.; Cruz, D.; Heil, T.; Arazoe, H.; Lova, P.; Aida, T.; Comoretto, D.; Patrini, M.; Antonietti, M. Shine Bright Like a Diamond: New Light on an Old Polymeric Semiconductor. *Adv. Mater.* **2020**, *32*, No. 1908140. (d) Xia, Y.; Tian, Z.; Heil, T.; Meng, A.; Cheng, B.; Cao, S.; Yu, J.; Antonietti, M. Highly Selective CO2 Capture and Its

Direct Photochemical Conversion on Ordered 2D/1D Heterojunctions. *Joule* **2019**, *3*, 2792−2805. (e) Li, A.; Cao, Q.; Zhou, G.; Schmidt, B. V.; Zhu, W.; Yuan, X.; Huo, H.; Gong, J.; Antonietti, M. Three-Phase Photocatalysis for the Enhanced Selectivity and Activity of CO2 Reduction on a Hydrophobic Surface. *Angew. Chem., Int. Ed.* **2019**, *58*, 14549−14697. (f) Das, S.; Murugesan, K.; Rodríguez, G. J. V.; Kaur, J.; Barham, J. P.; Savateev, A.; Antonietti, M.; König, B. Photocatalytic (Het)arylation of C(sp3)−H Bonds with Carbon Nitride. *ACS Catal.* **2021**, *11*, 1593−1603. (g) Zhang, Y.; Hatami, N.; Lange, N.; Schilling, W.; Ronge, E.; Jooss, C.; Das, S. A metal-free heterogeneous photocatalyst for the selective oxidative cleavage of C−C bonds in aryl olefins via harvesting direct solar energy. *Green Chem.* **2020**, *22*, 4516−4522.

(5) (a) Mohamed, M. A.; Zain, M.; Minggu, L. J.; Kassim, M. B.; Amin, N. A. S.; Salleh, W.; Salehmin, M. N. I.; Nasir, M. F. M.; Hir, Z. A. M. Constructing bio-templated 3D porous microtubular C-doped g-C3N4 with tunable band structure and enhanced charge carrier separation. *Appl. Catal., B* **2018**, *236*, 265−279. (b) Xu, Q.; Zhang, L.; Yu, J.; Wageh, S.; Al-Ghamdi, A. A.; Jaroniec, M. Direct Z-scheme photocatalysts: Principles, synthesis, and applications. *Mater. Today* **2018**, *21*, 1042−1063. (c) Liao, G.; Gong, Y.; Zhang, L.; Gao, H.; Yang, G.-J.; Fang, B. Semiconductor polymeric graphitic carbon nitride photocatalysts: the "holy grail" for the photocatalytic hydrogen evolution reaction under visible light. *Energy Environ. Sci.* **2019**, *12*, 2080−2147. (d) Ou, H.; Yang, P.; Lin, L.; Anpo, M.; Wang, X. Carbon Nitride Aerogels for the Photoredox Conversion of Water. *Angew. Chem., Int. Ed.* **2017**, *56*, 10905−10910. (e) Hou, H.; Zeng, X.; Zhang, X. Production of Hydrogen Peroxide by Photocatalytic Processes. *Angew. Chem., Int. Ed.* **2020**, *59*, 17356−17376.

(6) (a) Pei, Z.; Ding, L.; Hu, J.; Weng, S.; Zheng, Z.; Huang, M.; Liu, P. Defect and its dominance in ZnO films: A new insight into the role of defect over photocatalytic activity. *Appl. Catal., B* **2013**, *142*−*143*, 736−743. (b) Xiong, J.; Di, J.; Xia, J.; Zhu, W.; Li, H. Surface Defect Engineering in 2D Nanomaterials for Photocatalysis. *Adv. Funct. Mater.* **2018**, *28*, No. 1801983. (c) Li, Y.; Ho, W.; Lv, K.; Zhu, B.; Lee, S. C. Carbon vacancy-induced enhancement of the visible light-driven photocatalytic oxidation of NO over g-C3N4 nanosheets. *Appl. Surf. Sci.* **2018**, *430*, 380−389.

(7) (a) Goclon, J.; Winkler, K. Computational insight into the mechanism of O2 to H2O2 reduction on amino-groups-containing g-C3N4. *Appl. Surf. Sci.* **2018**, *462*, 134−141. (b) Li, X.; Zhang, J.; Zhou, F.; Zhang, H.; Bai, J.; Wang, Y.; Wang, H. Preparation of N-vacancy-doped g-C3N4 with outstanding photocatalytic H2O2 production ability by dielectric barrier discharge plasma treatment. *Chin. J. Catal.* **2018**, *39*, 1090−1098. (c) Shi, L.; Yang, L.; Zhou, W.; Liu, Y.; Yin, L.; Hai, X.; Song, H.; Ye, J. Photoassisted Construction of Holey Defective g-C3N4 Photocatalysts for Efficient Visible-Light-Driven H2O2 Production. *Small* **2018**, *14*, No. 1703142.

(8) (a) Cai, J.; Huang, J.; Wang, S.; Iocozzia, J.; Sun, Z.; Sun, J.; Yang, Y.; Lai, Y.; Lin, Z. Crafting Mussel-Inspired Metal Nanoparticle-Decorated Ultrathin Graphitic Carbon Nitride for the Degradation of Chemical Pollutants and Production of Chemical Resources. *Adv. Mater.* **2019**, *31*, No. 1806314. (b) Bellardita, M.; García-López, E. I.; Marcì, G.; Krivtsov, I.; García, J. R.; Palmisano, L. Selective photocatalytic oxidation of aromatic alcohols in water by using P-doped g-C3N4. *Appl. Catal., B* **2018**, *220*, 222−233. (c) Hu, J.; Zhang, P.; An, W.; Liu, L.; Liang, Y.; Cui, W. In-situ Fe-doped g-C3N4 heterogeneous catalyst via photocatalysis-Fenton reaction with enriched photocatalytic performance for removal of complex waste-water. *Appl. Catal., B* **2019**, *245*, 130−142. (d) Hu, S.; Qu, X.; Li, P.; Wang, F.; Li, Q.; Song, L.; Zhao, Y.; Kang, X. Photocatalytic oxygen reduction to hydrogen peroxide over copper doped graphitic carbon nitride hollow microsphere: The effect of Cu(I)-N active sites. *Chem. Eng. J.* **2018**, *334*, 410−418.

(9) (a) Qu, X.; Hu, S.; Bai, J.; Li, P.; Lu, G.; Kang, X. Synthesis of band gap-tunable alkali metal modified graphitic carbon nitride with outstanding photocatalytic H2O2 production ability via molten salt method. *J. Mater. Sci. Technol.* **2018**, *34*, 1932−1938. (b) Zhang, C.; Bai, J.; Ma, L.; Lv, Y.; Wang, F.; Zhang, X.; Yuan, X.; Hu, S. Synthesis of halogen doped graphite carbon nitride nanorods with outstanding photocatalytic H2O2 production ability via saturated NH4X (X = Cl, Br) solution-hydrothermal post-treatment. *Diamond Relat. Mater.* **2018**, *87*, 215−222. (c) Kim, S.; Moon, G.-h.; Kim, H.; Mun, Y.; Zhang, P.; Lee, J.; Choi, W. Selective charge transfer to dioxygen on KPF6-modified carbon nitride for photocatalytic synthesis of H2O2 under visible light. *J. Catal.* **2018**, *357*, 51−58.

(10) (a) Zhao, S.; Guo, T.; Li, X.; Xu, T.; Yang, B.; Zhao, X. Carbon nanotubes covalent combined with graphitic carbon nitride for photocatalytic hydrogen peroxide production under visible light. *Appl. Catal., B* **2018**, *224*, 725−732. (b) Tasis, D.; Tagmatarchis, N.; Bianco, A.; Prato, M. Chemistry of Carbon Nanotubes. *Chem. Rev.* **2006**, *106*, 1105−1136. (c) Zhao, S.; Zhao, X. Polyoxometalates-derived metal oxides incorporated into graphitic carbon nitride framework for photocatalytic hydrogen peroxide production under visible light. *J. Catal.* **2018**, *366*, 98−106. (d) Kofuji, Y.; Ohkita, S.; Shiraishi, Y.; Sakamoto, H.; Ichikawa, S.; Tanaka, S.; Hirai, T. Mellitic Triimide-Doped Carbon Nitride as Sunlight-Driven Photocatalysts for Hydrogen Peroxide Production. *ACS Sustainable Chem. Eng.* **2017**, *5*, 6478−6485. (e) Yang, L.; Dong, G.; Jacobs, D. L.; Wang, Y.; Zang, L.; Wang, C. Two-channel photocatalytic production of H2O2 over g-C3N4 nanosheets modified with perylene imides. *J. Catal.* **2017**, *352*, 274−281.

(11) (a) Ma, Z.; Lu, C.; Chen, J.; Rokicinska, A.; Kustrowski, P.; Coridan, R.; Dronskowski, R.; Slabon, A.; Jaworski, A. CeTiO2N oxynitride perovskite: paramagnetic 14N MAS NMR without para-magnetic shifts. *Z. Naturforsch. B* **2021**, *76*, 275−280. (b) Chen, Z.; Jaworski, A.; Chen, J.; Budnyak, T.; Szewczyk, I.; Rokicinska, A.; Dronskowski, R.; Hedin, N.; Kuśtrowski, P.; Slabon, A. Graphitic nitrogen in carbon catalysts is important for the reduction of nitrite as revealed by naturally abundant 15N NMR spectroscopy. *Dalton Trans.* **2021**, *50*, 6857−6866.

(12) (a) Fang, X.; Mao, J.; Levin, E. M.; Rohr, K. S. Nonaromatic Core−Shell Structure of Nanodiamond from Solid-State NMR Spectroscopy. *J. Am. Chem. Soc.* **2009**, *131*, 1426−1435. (b) Rossini, A. J.; Zagdoun, A.; Lelli, M.; Canivet, J.; Aguado, S.; Ouari, O.; Tordo, P.; Rosay, M.; Maas, W. E.; Copéret, C.; Farrusseng, D.; Emsley, L.; Lesage, A. Dynamic Nuclear Polarization Enhanced Solid-State NMR Spectroscopy of Functionalized Metal−Organic Frameworks. *Angew. Chem., Int. Ed.* **2012**, *51*, 123−127. (c) Rossini, A. J.; Widdifield, C. M.; Zagdoun, A.; Lelli, M.; Schwarzwälder, M.; Copéret, C.; Lesage, A.; Emsley, L. Dynamic Nuclear Polarization Enhanced NMR Spectroscopy for Pharmaceutical Formulations. *J. Am. Chem. Soc.* **2014**, *136*, 2324−2334. (d) Szewczyk, I.; Rokicińska, A.; Michalik, M.; Chen, J.; Jaworski, A.; Aleksis, R.; Pell, A. J.; Hedin, N.; Slabon, A.; Kuśtrowski, P. Electrochemical Denitrification and Oxidative Dehydrogenation of Ethylbenzene over N-doped Mesoporous Carbon: Atomic Level Understanding of Catalytic Activity by 15N NMR Spectroscopy. *Chem. Mater.* **2020**, *32*, 7263−7273. (e) Wei, Z.; Becwar, S. M.; Chmelka, B. F.; Sautet, P. Atomic Environments in N-Containing Graphitic Carbon Probed by First-Principles Calculations and Solid-State Nuclear Magnetic Resonance. *J. Phys. Chem. C* **2021**, *125*, 8779−8787.

(13) (a) van Duin, A. C. T.; Dasgupta, S.; Lorant, F.; Goddard, W. A., III ReaxFF: A Reactive Force Field for Hydrocarbons. *J. Phys. Chem. A* **2001**, *105*, 9396−9409. (b) Chenoweth, K.; van Duin, A. C. T.; Goddard, W. A., III ReaxFF Reactive Force Field for Molecular Dynamics Simulations of Hydrocarbon Oxidation. *J. Phys. Chem. A* **2008**, *112*, 1040−1053.

(14) (a) Ma, Y.; Yang, Y.; Lu, C.; Wen, X.; Liu, X.; Wu, S.; Lu, K.; Yin, J. Enhanced thermal resistance of carbon/phenolic composites by addition of novel nano-g-C3N4. *Compos. Sci. Technol.* **2019**, *180*, 60−70. (b) de Sousa, J. M.; Botari, T.; Perim, E.; Bizao, R. A.; Galvao, D. S. Mechanical and structural properties of graphene-like carbon nitride sheets. *RSC Adv.* **2016**, *6*, 76915−76921.

(15) De Santi, A.; Monti, S.; Barcaro, G.; Zhang, Z.; Barta, K.; Deuss, P. J. New Mechanistic Insights into the Lignin β-O-4 Linkage Acidolysis with Ethylene Glycol Stabilization Aided by Multilevel Computational Chemistry. *ACS Sustainable Chem. Eng.* **2021**, *9*, 2388−2399.

https://doi.org/10.1021/acscatal.1c03733
ACS Catal. XXXX, XXX, XXX−XXX

(16) (a) Campos-Martin, J. M.; Blanco-Brieva, G.; Fierro, J. L. Hydrogen Peroxide Synthesis: An Outlook beyond the Anthraquinone Process. *Angew. Chem., Int. Ed.* **2006**, *45*, 6962−6984. (b) Ksibi, M. Chemical oxidation with hydrogen peroxide for domestic wastewater treatment. *Chem. Eng. J.* **2006**, *119*, 161−165. (c) Gurram, R. N.; Al-Shannag, M.; Lecher, N. J.; Duncan, S. M.; Singsaas, E. L.; Alkasrawi, M. Bioconversion of paper mill sludge to bioethanol in the presence of accelerants or hydrogen peroxide pretreatment. *Bioresour. Technol.* **2015**, *192*, 529−539. (d) Zhan, W.; Ji, L.; Ge, Z.-m.; Wang, X.; Li, R.-t. A continuous-flow synthesis of primary amides from hydrolysis of nitriles using hydrogen peroxide as oxidant. *Tetrahedron* **2018**, *74*, 1527−1532.

(17) https://www.grandviewresearch.com/industry-analysis/hydrogen-peroxide-market (accessed 2021-07-06).

(18) (a) Edwards, J. K.; Hutchings, G. J. Palladium and Gold−Palladium Catalysts for the Direct Synthesis of Hydrogen Peroxide. *Angew. Chem., Int. Ed.* **2008**, *47*, 9192−9198. (b) García-Serna, J.; Moreno, T.; Biasi, P.; Cocero, M. J.; Mikkola, J.-P.; Salmi, T. O. Engineering in direct synthesis of hydrogen peroxide: targets, reactors and guidelines for operational conditions. *Green Chem.* **2014**, *16*, 2320−2343. (c) Yang, S.; Verdaguer-Casadevall, A.; Arnarson, L.; Silvioli, L.; Čolić, V.; Frydendal, R.; Rossmeisl, J.; Chorkendorff, I.; Stephens, I. E. L. Toward the Decentralized Electrochemical Production of H2O2: A Focus on the Catalysis. *ACS Catal.* **2018**, *8*, 4064−4081. (d) Haider, Z.; Cho, H.-i.; Moon, G.-h.; Kim, H.-i. Minireview: Selective production of hydrogen peroxide as a clean oxidant over structurally tailored carbon nitride photocatalysts. *Catal. Today* **2019**, *335*, 55−64.

(19) Kato, S.; Jung, J.; Suenobua, T.; Fukuzumi, S. Production of hydrogen peroxide as a sustainable solar fuel from water and dioxygen. *Energy Environ. Sci.* **2013**, *6*, 3756−3764.

(20) Kaynan, N.; Berke, B. A.; Hazut, O.; Yerushalmi, R. Sustainable photocatalytic production of hydrogen peroxide from water and molecular oxygen. *J. Mater. Chem. A* **2014**, *2*, 13822−13826.

(21) Wang, L.; Cao, S.; Guo, K.; Wu, Z.; Ma, Z.; Piao, L. Simultaneous hydrogen and peroxide production by photocatalytic water splitting. *Chin. J. Catal.* **2019**, *40*, 470−475.

(22) Shiraishi, Y.; Takii, T.; Hagi, T.; Mori, S.; Kofuji, Y.; Kitagawa, Y.; Tanaka, S.; Ichikawa, S.; Hirai, T. Resorcinol−formaldehyde resins as metal-free semiconductor photocatalysts for solar-to-hydrogen peroxide energy conversion. *Nat. Mater.* **2019**, *18*, 985−993.

(23) Shiraishi, Y.; Kanazawa, S.; Kofuji, Y.; Sakamoto, H.; Ichikawa, S.; Tanaka, S.; Hirai, T. Sunlight-Driven Hydrogen Peroxide Production from Water and Molecular Oxygen by Metal-Free Photocatalysts. *Angew. Chem., Int. Ed.* **2014**, *53*, 13454−13459.

(24) (a) Maurino, V.; Minero, C.; Mariella, G.; Pelizzetti, E. Sustained production of H2O2 on irradiated TiO2 − fluoride systems. *Chem. Commun.* **2005**, 2627−2629. (b) Maurino, V.; Minero, C.; Pelizzetti, E.; Mariella, G.; Arbezzano, A.; Rubertelli, F. Influence of Zn(II) adsorption on the photocatalytic activity and the production of H2O2 over irradiated TiO2. *Res. Chem. Intermed.* **2007**, *33*, 319−332. (c) Teranishi, M.; Naya, S.; Tada, H. In Situ Liquid Phase Synthesis of Hydrogen Peroxide from Molecular Oxygen Using Gold Nanoparticle-Loaded Titanium(IV) Dioxide Photocatalyst. *J. Am. Chem. Soc.* **2010**, *132*, 7850−7851.

(25) (a) Zeng, X.; Wang, Z.; Meng, N.; McCarthy, D. T.; Deletic, A.; Pan, J.-h.; Zhang, X. Highly dispersed TiO2 nanocrystals and carbon dots on reduced graphene oxide: Ternary nanocomposites for accelerated photocatalytic water disinfection. *Appl. Catal., B* **2017**, *202*, 33−41. (b) Zeng, X.; Wang, Z.; Wang, G.; Gengenbach, T. R.; McCarthy, D. T.; Deletic, A.; Yu, J.; Zhang, X. Highly dispersed TiO2 nanocrystals and WO3 nanorods on reduced graphene oxide: Z-scheme photocatalysis system for accelerated photocatalytic water disinfection. *Appl. Catal., B* **2017**, *218*, 163−173. (c) Zheng, L.; Su, H.; Zhang, J.; Walekar, L. S.; Vafaei Molamahmood, H.; Zhou, B.; Long, M.; Hu, Y. H. Highly selective photocatalytic production of H2O2 on sulfur and nitrogen co-doped graphene quantum dots tuned TiO2. *Appl. Catal., B* **2018**, *239*, 475−484.

(26) (a) Sun, Y.; Cheng, J. Hydrolysis of lignocellulosic materials for ethanol production: a review. *Bioresour. Technol.* **2002**, *83*, 1−11. (b) Álvarez, C.; Sosa, F. M. R.; Díez, B. Enzymatic hydrolysis of biomass from wood. *Microb. Biotechnol.* **2016**, *9*, 149−156.

(27) Moon, G.-h.; Kim, W.; Bokare, A. D.; Sung, N.-e.; Choi, W. Solar production of H2O2 on reduced graphene oxide−TiO2 hybrid photocatalysts consisting of earth-abundant elements only. *Energy Environ. Sci.* **2014**, *7*, 4023−4028.

(28) Isaka, Y.; Kawase, Y.; Kuwahara, Y.; Mori, K.; Yamashita, Y. Two-Phase System Utilizing Hydrophobic Metal−Organic Frameworks (MOFs) for Photocatalytic Synthesis of Hydrogen Peroxide. *Angew. Chem., Int. Ed.* **2019**, *58*, 5402−5406.

(29) Krishnaraj, C.; Jena, H. S.; Bourda, L.; Laemont, A.; Pachfule, P.; Roeser, J.; Chandran, C. V.; Borgmans, S.; Rogge, S. M. J.; Leus, K.; Stevens, C. V.; Martens, J. A.; Speybroeck, V. V.; Breynaert, E.; Thomas, A.; van Der Voort, P. Strongly Reducing (Diarylamino)benzene-Based Covalent Organic Framework for Metal-Free Visible Light Photocatalytic H2O2 Generation. *J. Am. Chem. Soc.* **2020**, *142*, 20107−20116.

(30) (a) Zeng, X.; Liu, Y.; Kang, Y.; Li, Q.; Xia, Y.; Zhu, Y.; Hou, H.; Uddin, H.; Gengenbach, T. R.; Xia, D.; Sun, C.; Mccarthy, D. T.; Deletic, A.; Yu, J.; Zhang, X. Simultaneously Tuning Charge Separation and Oxygen Reduction Pathway on Graphitic Carbon Nitride by Polyethylenimine for Boosted Photocatalytic Hydrogen Peroxide Production. *ACS Catal.* **2020**, *10*, 3697−3706. (b) Ye, Y.-X.; Pan, J.; Xie, F.; Gong, L.; Huang, S.; Ke, Z.; Zhu, F.; Xu, J.; Ouyang, G. Highly efficient photosynthesis of hydrogen peroxide in ambient conditions. *Proc. Natl. Acad. Sci. U.S.A.* **2021**, *118*, No. e2103964118. (c) Fu, Y.; Liu, C.; Zhang, M.; Zhu, C.; Li, H.; Wang, H.; Song, Y.; Huang, H.; Liu, Y.; Kang, Z. Photocatalytic H2O2 and H2 Generation from Living Chlorella vulgaris and Carbon Micro Particle Comodified g-C3N4. *Adv. Energy Mater.* **2018**, *8*, No. 1802525.

(31) (a) Chu, C.; Zhu, Q.; Pan, Z.; Gupta, S.; Huang, D.; Du, Y.; Weon, S.; Wu, Y.; Muhich, C.; Stavitski, E.; Domen, K.; Kim, J.-H. Spatially separating redox centers on 2D carbon nitride with cobalt single atom for photocatalytic H2O2 production. *Proc. Natl. Acad. Sci. U.S.A.* **2020**, *117*, 6376−6382. (b) Oka, K.; Nishide, H.; Jensen, B. W. Copolymer of Phenylene and Thiophene toward a Visible-Light-Driven Photocatalytic Oxygen Reduction to Hydrogen Peroxide. *Adv. Sci.* **2021**, *8*, No. 2003077. (c) Chen, L.; Wang, L.; Wan, Y.; Zhang, Y.; Qi, Z.; Wu, X.; Xu, H. Acetylene and Diacetylene Functionalized Covalent Triazine Frameworks as Metal-Free Photocatalysts for Hydrogen Peroxide Production: A New Two-Electron Water Oxidation Pathway. *Adv. Mater.* **2020**, *32*, No. 1904433. (d) Gryszel, M.; Rybakiewicz, R.; Głowacki, E. D. Water-Soluble Organic Dyes as Molecular Photocatalysts for H2O2 Evolution. *Adv. Sustainable Syst.* **2019**, *3*, No. 1900027.

(32) Shiraishi, Y.; Kanazawa, S.; Sugano, Y.; Tsukamoto, D.; Sakamoto, H.; Ichikawa, S.; Hirai, T. Highly Selective Production of Hydrogen Peroxide on Graphitic Carbon Nitride (g-C3N4) Photocatalyst Activated by Visible Light. *ACS Catal.* **2014**, *4*, 774−780.

(33) Shiraishi, Y.; Kofuji, Y.; Sakamoto, H.; Tanaka, S.; Ichikawa, S.; Hirai, T. Effects of Surface Defects on Photocatalytic H2O2 Production by Mesoporous Graphitic Carbon Nitride under Visible Light Irradiation. *ACS Catal.* **2015**, *5*, 3058−3066.

(34) Moon, G.-h.; Fujitsuka, M.; Kim, S.; Majima, T.; Wang, X.; Choi, W. Eco-Friendly Photochemical Production of H2O2 through O2 Reduction over Carbon Nitride Frameworks Incorporated with Multiple. *ACS Catal.* **2017**, *7*, 2886−2895.

(35) Peng, Y.; Wang, L.; Liu, Y.; Chen, H.; Lei, J.; Zhang, J. Visible-Light-Driven Photocatalytic H2O2 Production on g-C3N4 Loaded with CoP as a Noble Metal Free Cocatalyst. *Eur. J. Inorg. Chem.* **2017**, *2017*, 4797−4802.

(36) Chang, X.; Yang, J.; Han, D.; Zhang, B.; Xiang, X.; He, J. Enhancing Light-Driven Production of Hydrogen Peroxide by Anchoring Au onto C3N4 Catalysts. *Catalysts* **2018**, *8*, No. 147.

(37) Zhao, S.; Zhao, X.; Zhang, H.; Li, J.; Zhu, Y. Covalent combination of polyoxometalate and graphitic carbon nitride for light-driven hydrogen peroxide production. *Nano Energy* **2017**, *35*, 405−414.

https://doi.org/10.1021/acscatal.1c03733
ACS Catal. XXXX, XXX, XXX−XXX

(38) Kim, H.-i.; Choi, Y.; Hu, S.; Choi, W.; Kim, J.-H. Photocatalytic hydrogen peroxide production by anthraquinone-augmented polymeric carbon nitride. *Appl. Catal., B* **2018**, *229*, 121−129.
(39) Kim, S.; Moon, G.-h.; Kim, H.; Mun, Y.; Zhang, P.; Lee, J.; Choi, W. Selective charge transfer to dioxygen on KPF6-modified carbon nitride for photocatalytic synthesis of H2O2 under visible light. *J. Catal.* **2018**, *357*, 51−58.
(40) Li, X.; Zhang, J.; Zhou, F.; Zhang, H.; Bai, J.; Wang, Y.; Wang, H. Preparation of N-vacancy-doped g-C3N4 with outstanding photocatalytic H2O2 production ability by dielectric barrier discharge plasma treatment. *Chin. J. Catal.* **2018**, *39*, 1090−1098.
(41) Qu, X.; Hu, S.; Li, P.; Li, Z.; Wang, H.; Ma, H.; Li, W. The effect of embedding N vacancies into g-C3N4 on the photocatalytic H2O2 production ability via H2 plasma treatment. *Diamond Relat. Mater.* **2018**, *86*, 159−166.
(42) Wang, R.; Zhang, X.; Li, F.; Cao, D.; Pu, M.; Han, D.; Yang, J.; Xiang, X. Energy-level dependent H2O2 production on metal-free, carbon-content tunable carbon nitride photocatalysts. *J. Energy Chem.* **2018**, *27*, 343−350.
(43) Wei, Z.; Liu, M.; Zhang, Z.; Yao, W.; Tan, H.; Zhu, Y. Efficient visible-light-driven selective oxygen reduction to hydrogen peroxide by oxygen-enriched graphitic carbon nitride polymers. *Energy Environ. Sci.* **2018**, *11*, 2581−2589.
(44) Zhao, S.; Zhao, X.; Ouyang, S.; Zhu, Y. Polyoxometalates covalently combined with graphitic carbon nitride for photocatalytic hydrogen peroxide production. *Catal. Sci. Technol.* **2018**, *8*, 1686−1695.
(45) Tian, J.; Wu, T.; Wang, D.; Pei, Y.; Qiao, M.; Zong, B. One-pot synthesis of potassium and phosphorus-doped carbon nitride catalyst derived from urea for highly efficient visible light-driven hydrogen peroxide production. *Catal. Today* **2019**, *330*, 171−178.
(46) Zhao, S.; Zhao, X. Insights into the role of singlet oxygen in the photocatalytic hydrogen peroxide production over polyoxometalates-derived metal oxides incorporated into graphitic carbon nitride framework. *Appl. Catal., B* **2019**, *250*, 408−418.
(47) Zuo, G.; Liu, S.; Wang, L.; Song, H.; Zong, P.; Hou, W.; Li, B.; Guo, Z.; Meng, X.; Du, Y.; Wang, T.; Roy, V. A. L. Finely dispersed Au nanoparticles on graphitic carbon nitride as highly active photocatalyst for hydrogen peroxide production. *Catal. Commun.* **2019**, *123*, 69−72.
(48) Wu, S.; Yu, H.; Chen, S.; Quan, X. Enhanced Photocatalytic H2O2 Production over Carbon Nitride by Doping and Defect Engineering. *ACS Catal.* **2020**, *10*, 14380−14389.
(49) Yang, Y.; Zeng, Z.; Zeng, G.; Huang, D.; Xiao, R.; Zhang, C.; Zhou, C.; Xiong, W.; Wang, W.; Cheng, M.; Xue, W.; Guo, H.; Tang, X.; He, D. Ti3C2 Mxene/porous g-C3N4 interfacial Schottky junction for boosting spatial charge separation in photocatalytic H2O2 production. *Appl. Catal., B* **2019**, *258*, No. 117956.
(50) Yang, Y.; Zhang, C.; Huang, D.; Zeng, G.; Huang, J.; Lai, C.; Zhou, C.; Wang, W.; Guo, H.; Xue, W.; Deng, R.; Cheng, M.; Xiong, W. Boron nitride quantum dots decorated ultrathin porous g-C3N4: Intensified exciton dissociation and charge transfer for promoting visible-light-driven molecular oxygen activation. *Appl. Catal., B* **2019**, *245*, 87−99.
(51) Zhang, P.; Tong, Y.; Liu, Y.; Vequizo, J. J. M.; Sun, H.; Yang, C.; Yamakata, A.; Fan, F.; Lin, W.; Wang, X.; Choi, W. Heteroatom Dopants Promote Two-Electron O2 Reduction for Photocatalytic Production of H2O2 on Polymeric Carbon Nitride. *Angew. Chem., Int. Ed.* **2020**, *59*, 16209−16217.
(52) Hu, Y.; Shim, Y.; Oh, J.; Park, S.; Park, S.; Ishii, Y. Synthesis of 13C-,15N-Labeled Graphitic Carbon Nitrides and NMR-Based Evidence of Hydrogen-Bonding Assisted Two-Dimensional Assembly. *Chem. Mater.* **2017**, *29*, 5080−5089.
(53) Sehnert, J.; Baerwinkel, K.; Senker, J. Ab Initio Calculation of Solid-State NMR Spectra for Different Triazine and Heptazine Based Structure Proposals of g-C3N4. *J. Phys. Chem. B* **2007**, *111*, 10671−10680.
(54) Fukaya, H.; Ono, T. DFT-GIAO calculations of 19F NMR chemical shifts for perfluoro compounds. *J. Comput. Chem.* **2004**, *25*, 51−60.
(55) Sun, Y.-N.; Yang, J.; Ding, X.; Ji, W.; Jaworski, A.; Hedin, N.; Han, B.-H. Synergetic contribution of nitrogen and fluorine species in porous carbons as metal-free and bifunctional oxygen electrocatalysts for zinc−air batteries. *Appl. Catal., B* **2021**, *297*, No. 120448.
(56) (a) Stoychev, G. L.; Auer, A. A.; Neese, F. Efficient and Accurate Prediction of Nuclear Magnetic Resonance Shielding Tensors with Double-Hybrid Density Functional Theory. *J. Chem. Theory Comput.* **2018**, *14*, 4756. (b) Rzepka, P.; Bacsik, Z.; Pell, A. J.; Hedin, N.; Jaworski, A. Nature of Chemisorbed CO2 in Zeolite A. *J. Phys. Chem. C* **2019**, *123*, 21497−21503.
(57) Sobańska, K.; Pietrzyk, P.; Sojka, Z. Generation of Reactive Oxygen Species via Electroprotic Interaction of H2O2 with ZrO2 Gel: Ionic Sponge Effect and pH-Switchable Peroxidase- and Catalase-Like Activity. *ACS Catal.* **2017**, *7*, 2935−2947.
(58) Reszka, K.; Chignell, C. F. Spectroscopic studies of cutaneous photosensitizing agents-IV. The photolysis of benoxaprofen, an anti-inflammatory drug with phototoxic properties. *Photochem. Photobiol.* **1983**, 281.
(59) Bilski, P.; Chignell, C. F.; Szychlinski, J.; Borkowski, A.; Oleksy, E.; Reszka, K. Photooxidation of organic and inorganic substrates during UV photolysis of nitrite anion in aqueous solution. *J. Am. Chem. Soc.* **1992**, *114*, 549−556.

https://doi.org/10.1021/acscatal.1c03733
ACS Catal. XXXX, XXX, XXX−XXX